Time double-slit interferences in strong-field tunneling ionization

Diego G. Arbó,[1,2] Emil Persson,[1] and Joachim Burgdörfer[1]
[1]*Institute for Theoretical Physics, Vienna University of Technology, Wiedner Hauptstraße 8-10/136, A-1040 Vienna, Austria*
[2]*Institute for Astronomy and Space Physics, IAFE, CC 67, Suc. 28 (1428) Buenos Aires, Argentina*
(Received 22 September 2006; published 14 December 2006)

Oscillations in the electron emission spectrum of atoms ionized by few-cycle laser pulses were recently identified as a time double-slit interference [F. Lindner *et al.*, Phys. Rev. Lett. **95**, 040401 (2005)]. We extend this analysis to three-dimensional momentum images. We show that different portions of the wave packet released at different times interfere, forming interference fringes in the momentum distributions. The complex interference pattern observable in momentum space maps out information on the scattering potential.

DOI: 10.1103/PhysRevA.74.063407 PACS number(s): 32.80.Rm, 32.80.Fb, 03.65.Sq

I. INTRODUCTION

The generation of few-cycle optical pulses with duration τ of less than 10 fs corresponding to fewer than four cycles has become routine in several laser laboratories [1–4]. Ultrashort pulses for which τ becomes comparable to the optical period associated with the carrier frequency lead to novel features of laser-matter interactions; among them are the strong carrier-envelope (CE) phase dependence of excitation and ionization processes [5,6]. Another consequence is that electron emission, which in the tunnel ionization regime occurs near the maxima of the electric field, is temporally confined to a few adjacent field maxima. The interference between such ionization bursts gives rise to features in the electron emission spectrum dP/dE markedly different from the typical above-threshold ionization (ATI) spectrum for longer pulses with well-defined ponderomotive energy [7–12]. Lindner *et al.* [13] have recently demonstrated that an ultrashort pulse with a sinelike shape gives rise to a double-slit interference in time. Two electron bursts ejected at times of different field maxima and detected along the polarization axis generate interference fringes in the emitted electron energy spectra. The fringe pattern was shown to be strongly dependent on the carrier-envelope phase when switching from a sinelike to a cosinelike pulse shape. The latter effectively closes one of the two slits. Thus, the variation of the carrier-envelope phase allows one to tune the degree of "which-way" information available. Moreover, a strong directional dependence of the fringe pattern was observed.

In the present communication we extend this study of the time double-slit interference emission pattern to the two-dimensional (2D) momentum distribution of the outgoing electron along the direction of the laser polarization, k_z, and the perpendicular polar coordinate k_ρ. The two-dimensional distribution reveals a complex diffraction pattern which can provide information on both the laser-driven emission process and the scattering potential. We point out that the interference of two electron microbursts emitted from an atomic "point" source allows one, in principle, to holographically image the effective atomic potential the receding electron experiences. We present both full numerical solutions of the time-dependent Schrödinger equation (TDSE) as well as a simple analytic semiclassical model closely following the "simple man's model" [14–16] for ultrashort pulses subtending one to two pulses. Atomic units are used throughout.

II. METHODS

We consider a hydrogen atom interacting with a linearly polarized laser field. The Hamiltonian of the system is

$$H = \frac{\vec{p}^2}{2} + V(r) + zF(t), \tag{1}$$

where $V(r) = -1/r$ is the Coulomb potential energy, $\vec{p}$ and $\vec{r}$ are the momentum and position of the electron, respectively, and $\vec{F}(t)$ is the time-dependent external field linearly polarized along the $\hat{z}$ direction. The laser pulse is chosen to be of the form

$$\vec{F}(t) = f(t)\cos(\omega t + \phi_{CE})\hat{z}, \tag{2}$$

where ω is the laser carrier frequency, $f(t)$ is the envelope function, and ϕ_{CE} the relative carrier-envelope phase. For $f(t)$ we use the following two forms:

$$f(t) = F_0 \cos^2(\pi t/\tau)\theta(\tau/2 - |t|), \tag{3a}$$

$$f(t) = F_0 \theta(\tau/2 - |t|), \tag{3b}$$

where τ is the total pulse duration and $t=0$ corresponds to the middle of the pulse. $\phi_{CE}=0$ in Eq. (2) corresponds to a cosinelike pulse while $\phi_{CE}=\pm\pi/2$ corresponds to a $\mp$ sine pulse. While the form, Eq. (3a), can be considered a realistic approximation to the envelope of an ultrashort few-cycle pulse produced in a laboratory, Eq. (3b) is a convenient choice, allowing for analytic approximations, and facilitates insights into the buildup of interference patterns.

A. TDSE calculations

The time-dependent Schrödinger equation is solved by means of the generalized pseudospectral method [17]. The method combines a discretization of the radial coordinate optimized for the Coulomb singularity with quadrature methods to achieve stable long-time evolution using a split-operator method. It allows for an accurate description of both the unbound as well as the bound parts of the wave function

$|\psi(t)\rangle$. The process of detecting an electron of momentum $\vec{k}$ can then be viewed as a projection of the wave function after the laser pulse is turned off onto Coulomb waves [18–20]. Therefore, the asymptotic momentum distributions are obtained:

$$\frac{dP}{d\vec{k}} = \frac{1}{4\pi k}\left|\sum_l e^{i\delta_l(k)}\sqrt{2l+1}P_l(\cos\theta_k)\langle k,l|\psi(\tau)\rangle\right|^2, \quad (4)$$

where $\delta_l(k)$ is the momentum-dependent Coulomb phase shift, θ_k is the angle between $\vec{k}$ and the polarization direction $\hat{z}$ of the laser field, P_l is the Legendre polynomial of degree l, and $|k,l\rangle$ is the eigenstate of the free atomic Hamiltonian with positive eigenenergy $E=k^2/2$ and orbital quantum number l. The Coulomb projection is required for observables that are not constants of motion of the free evolution once the external field is turned off. Unlike the case of the photoelectron spectrum studied previously where the energy is a constant of motion of the free evolution, the asymptotic vectorial linear momentum discussed in the present paper requires the projection onto Coulomb waves. Cylindrical symmetry makes the dynamics a two-dimensional problem. The projection of the angular momentum on the polarization direction of the laser is a constant of motion (the magnetic quantum number m is unaffected during the time evolution). As the initial state of the system we consider the ground state of the hydrogen atom—i.e., $m=0$.

B. Semiclassical model

We analyze the interference pattern to be discussed below in terms of a "which-way" description with the help of a semiclassical model for the field shown in Fig. 1(a). We closely follow the Lewenstein [15] model to arrive to the "simple man's model." Briefly, in order to approximately solve the Schrödinger equation with the Hamiltonian given by Eq. (1) we use the following ansatz:

$$|\psi(t)\rangle = e^{iI_p t}\left[a(t)|0\rangle + \int d\vec{v}\, b(\vec{v},t)|\vec{v}\rangle\right], \quad (5)$$

where $|\vec{v}\rangle$ is an eigenstate of the continuous spectrum with velocity $\vec{v}$ and I_p is the atomic ionization potential ($I_P=0.5$ for the hydrogen case). Inserting Eq. (5) into the Schrödinger equation we arrive at the following expression for the amplitude of the continuum states:

$$b(\vec{k},t) = -\sum_{i=1}^{2}\left[\frac{2\pi i F(t_{SP}^{(i)})}{|\vec{k}+\vec{A}(t_{SP}^{(i)})|}\right]^{1/2} d^*[\vec{k}+\vec{A}(t_{SP}^{(i)})]e^{iS(t_{SP}^{(i)},t)}, \quad (6)$$

where, according to the strong-field approximation (SFA), S accounts for the Volkov action,

$$S(t',t) = -\int_{t'}^{t} dt''\left[\frac{[\vec{k}+\vec{A}(t'')]^2}{2} + I_p\right], \quad (7)$$

$d^*(\vec{v})=\langle\vec{v}|z|0\rangle$ is the dipole element of the bound-continuum transition, $\vec{A}(t)=-\int_0^t dt'\vec{F}(t')$ is the vector potential of the laser field divided by the speed of light, and $\vec{k}$ is the canonical momentum, $\vec{k}=\vec{v}(t)-\vec{A}(t)$. To arrive at Eq. (6) one employs

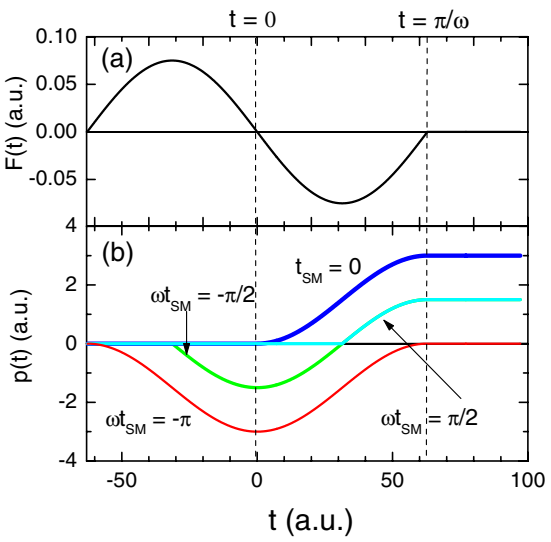

FIG. 1. (Color online) (a) Electric field of frequency $\omega=0.05$, duration $\tau=2\pi/\omega=126$ a.u., and amplitude $F_0=0.075$ a.u. as a function of time (one cycle corresponding to a square envelope function). (b) Momentum for different classical trajectories: electron detached at time $t=-\pi/\omega$, $-\pi/2\omega$, 0, $\pi/2\omega$, and π/ω, as indicated. The momenta of the trajectories of electrons released at $t=\mp\pi/2\omega$ coincide in the time interval $t\geqslant\pi/2\omega$ and give rise to interferences.

$\langle\vec{v}|\vec{v}'\rangle=\delta(\vec{v}-\vec{v}')$ and the following approximations: (i) the depletion of the ground state is neglected [$a(t)=1$], (ii) continuum-continuum transitions are of the form $\langle\vec{v}|z|\vec{v}'\rangle = i\nabla_v\delta(\vec{v}-\vec{v}')$, and (iii) the saddle-point approximation [21]. $t_{SP}^{(i)}$ $(i=1,2)$ are the complex solutions of the equation for the stationary phase action $\frac{\partial S(t'=t_{SP},t)}{\partial t'}=0$:

$$t_{SP}^{(1)} = \frac{1}{\omega}\cos^{-1}\left[1-(k_z \mp i\sqrt{2I_p+k_\rho^2})\frac{\omega}{F_0}\right] - \frac{\pi}{\omega}, \quad (8a)$$

$$t_{SP}^{(2)} = -t_{SP}^{(1)}. \quad (8b)$$

The photoelectron spectrum can be written as $\frac{dP}{dE} = 2\pi\int_{-1}^{1} d\cos\theta_k\sqrt{2E}|b(\vec{k},t=\pi/\omega)|^2$, since the energy is a constant of motion of the free evolution after the electric pulse is turned off. Thus, the energy distribution is invariant when taking the asymptotic limit. The same does not hold true, in general, for the final linear momentum. However, in the strong-field approximation in which the atomic core potential is neglected in the continuum state of the receding electron, the momentum distribution remains unchanged as well. Consequently, the momentum distribution $\frac{dP}{d\vec{k}}=|b(\vec{k},t=\pi/\omega)|^2$ can be written as

$$|b(\vec{k},t=\pi/\omega)|^2 = B(\vec{k})\cos^2[\Delta S(\vec{k})], \quad (9)$$

where the phase $\Delta S(\vec{k})=S(t_{SP}^{(2)},t)-S(t_{SP}^{(1)},t)$ controls the interference and the factor $B(\vec{k})$ is the ionization probability at a time $t_{SP}^{(i)}$. By making use of the simplified version of the saddle point method, where the ionization times of Eq. (8)

are considered real—i.e., $t_{SM}^{(i)}=\mathrm{Re}(t_{SP}^{(i)})$—the ionization probability can be written as [16]

$$B(\vec{k}) = \frac{\pi^2}{2(2I_p + k_\rho^2)|F(t(\vec{k}))|^2} \exp\left[-\frac{2(2I_p + k_\rho^2)^{3/2}}{3|F(t(\vec{k}))|} \right]. \tag{10}$$

Using $t_{SM}^{(i)}$ instead of $t_{SP}^{(i)}$ together with the assumption that the electron is detached from the nucleus at times $t_{SM}^{(i)}$ with zero velocity leads to the simple man's model [22]. The two emission times $t_{SM}^{(1)}$ and $t_{SM}^{(2)}$ correspond to two different classical trajectories that interfere when reaching the same final momentum. From the classical equations of motion, it follows that the detached electron acquires the longitudinal momentum

$$p(t) = \frac{F_0}{\omega}(\cos\,\omega t_{SM}^{(i)} - \cos\,\omega t). \tag{11}$$

Here, the effect of the atomic potential on the detached electron is neglected (SFA). The momentum $p(t)$ converges to the longitudinal momentum k_z in the limit $t\to\infty$ since in Eq. (11), $k_z=p(t\to\infty)=p(\pi/\omega)$.

The atom is predominantly ionized at the extremes of the one-cycle electric field—i.e., $\omega t_{SM}^{(i)}=\pm\pi/2$. For these trajectories, Eq. (11) leads to $p(t)=-(F_0/\omega)\cos\,\omega t$ (see Fig. 1). After one half-cycle pulse ($\tau=\pi/\omega$) the momentum of the electron is $p(0)=-F_0/\omega$, and after a complete-cycle pulse ($\tau=2\pi/\omega$), $p(\pi/\omega)=F_0/\omega$ [see Fig. 1(b)]. Thus the maximum intensity of ejected electrons is reached at $|p|=F_0/\omega$. The limiting cases for the smallest momenta are trajectories of the electron released right at the beginning (or end) of the pulse near $t=-\pi/2\omega$ (or $+\pi/\omega$) leading to $k_z=0$. The highest momentum $k_z=2F_0/\omega$ is reached for emission near $t=0$ which is the point of coalescence between the "long" trajectory emitted in the first half-cycle and the "short" trajectory emitted in the second half of the cycle. These trajectories are well known from high-harmonic generation and play also a crucial role in the buildup of interference patterns in the electron momentum image.

Figure 1(b) displays an example of two different trajectories released at times $t=-\pi/2\omega$ and $\pi/2\omega$ having the same final momentum. It is straightforward from Eq. (11) to find pairs of trajectories with the same final momentum. They obey the relation (8b), which is exactly the condition for interference of two classical trajectories in the Lewenstein model. The two emission times $t_{SM}^{(1,2)}$ therefore characterize the classical trajectories that are allowed to semiclassically interfere. From Fig. 1(b) it can be directly seen that the range of momenta for which classical trajectories are available for interference is constrained to values $0<p<2F_0/\omega$.

In the following section we compare and contrast the results of this simple semiclassical model and the full TDSE for the 2D momentum distribution created by an ultrashort one- and two-cycle pulse.

III. RESULTS AND DISCUSSION

At first, we consider pulses with the envelope function [Eq. (3a)], which corresponds to a realistic ultrashort pulse

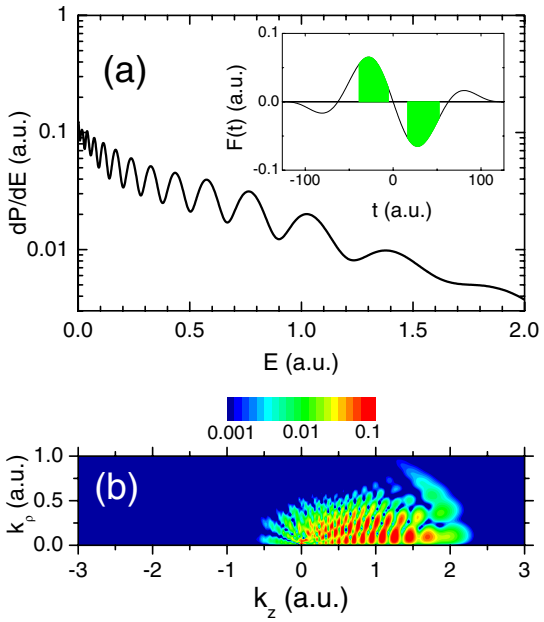

FIG. 2. (Color online) (a) *Ab initio* photoelectron spectra for a two-cycle electric field of frequency $\omega=0.05$ a.u., peak field $F_0=0.075$ a.u., and duration $\tau=4\pi/\omega=251$ (with a $\cos^2$ envelope function). Inset: electric field as a function of time. The shaded areas correspond to the two temporal slits. (b) Doubly differential electron momentum distribution in cylindrical coordinates (k_z,k_ρ) in logarithmic scale for the same laser pulse.

containing about two optical cycles and different CE phases. The inset of Fig. 2(a) displays the pulse with carrier frequency $\omega=0.05$, peak field $F_0=0.075$, which corresponds to an intensity of $I=2\times10^{14}$ W/cm^2 with duration $\tau=251$ a.u. and $\phi_{CE}=\pi/2$ (a sine-shaped pulse). For this pulse shape, only two paths effectively contribute to the ionization spectrum. The shaded areas show the two temporal slits where the ionization predominately occurs.

The photoelectron spectrum, shown in Fig. 2(a), has a nonequally spaced peak distribution and the separation between two consecutive peaks increases with energy. The peaks correspond to the time double-slit interference fringes observed by Lindner *et al.* [13]. Recent simulations [16] have also shown the existence of these peaks in the density probabilities at different angles of ejection but for a much stronger field (10^{16} W cm^{-2}) applied to He$^+$ atoms.

We extend the analysis of the fringe pattern to the doubly-differential momentum distribution $\frac{d^2P}{dk_\rho dk_z}$, which is plotted in Fig. 2(b) as a function of the final longitudinal, k_z, and transversal momentum of the electron, $k_\rho=\sqrt{k_x^2+k_y^2}$. Several characteristics of the two-dimensional distribution are noteworthy: (i) about 95% of the distribution lies in the region of positive longitudinal momentum ($k_z>0$), (ii) the distribution is constrained to the region $-0.5\lesssim k_z\lesssim 2.5$ and $k_\rho\lesssim 0.6$, and (iii) the distribution features an intricate nodal pattern that changes from a radial-circular nodal pattern near threshold to an almost vertical striplike pattern at larger k_z, slightly bent outward with increasing k_ρ at larger momenta. The near-threshold pattern has been recently analyzed for a multicycle pulse in terms of generalized Ramsauer-Townsend diffrac-

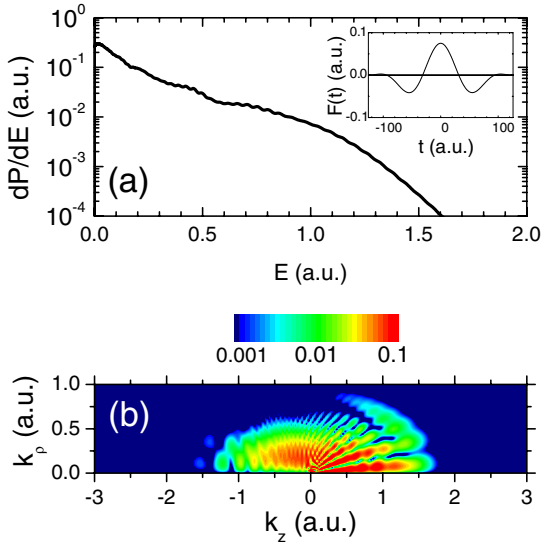

FIG. 3. (Color online) Same as Fig. 2 but for a cosine-envelope pulse, all other parameters unchanged.

tion oscillations [8], where Coulomb scattering effects have been shown to be important.

One key feature of the diffraction pattern for the sinelike shape pulse is the strong momentum asymmetry which underlies the "stereo ATI" technique to determine the carrier envelope phase [5]. Switching to a cosinelike pulse ($\phi_{CE}=0$) the asymmetry is much reduced [Fig. 3(b)]. Moreover, the oscillatory pattern in the photoelectron spectrum has disappeared [Fig. 3(a)]. This, however, does not imply that all the interference fringes are absent. On the contrary, they are well pronounced with radial atomic lines emanating from the origin. In other words, the doubly differential distribution is a smooth, almost structureless, function of the energy but an oscillatory function of the ejection angle. The latter corresponds to Ramsauer-Townsend diffraction fringes in the angular distributions [8]. The fringes are more pronounced in the forward hemisphere ($k_z>0$), indicating the importance of the positive half-cycle and the second negative half-cycle of the pulse [Fig. 3(a), inset] for creating the phase difference between interfering trajectories.

In order to simplify the analysis and to allow for an analytic treatment we choose now the rectangular envelope function subtending one optical-cycle function and consider the spectrum after one half cycle and a full cycle (Fig. 4). The distribution after a full cycle [Fig. 4(c)] can be compared with Fig. 2(b). The structural similarity reflects the fact that the two additional weak half-cycles of the driving field present in the inset of Fig. 2(a) but not in Fig. 1(a) lead only to a minor change of the 2D distribution. The total ionization probability, which can be calculated as the integral over the energy distribution [Fig. 4(a)], is higher for a full-cycle pulse than for a half-cycle pulse, as expected. After half a cycle the ionization probability is 0.06, while after a full-cycle pulse it is 0.12. This shows that the system is in the linear ionization regime very far away from the saturation limit. The depletion of the ground state is not yet important. The latter is one ingredient of the semiclassical formula, Eq. (9). The energy and 2D momentum distribution after a half-cycle is completely smooth [Figs. 4(a) and 4(b)] and the wave packet propagates in the negative z momentum direction [Fig. 4(b)]. In turn, when a second half-cycle acts on the electron, the wave packet moves towards the positive direction and a clear fringe pattern appears since a second slit has opened. Obviously, the two half-cycles (or portions thereof) act as the two slits of a time double-slit experiment. The wave packet is spread about 3 a.u. in the positive longitudinal momentum direction, about only 0.5 a.u. (17%) in the transverse momentum. A pulse subtending only one half-cycle [Fig. 4(b)] obviously does not correspond to a propagating wave of the electromagnetic fields. Pulse shapes that resemble half-cycle pulses have been created in the subpicosecond [23] and subnanosecond [24] regimes, the latter of which by conventional electronic pulse generators. Recently, a method to produce half-cycle pulses in the subfemtosecond regime has been proposed [25]. On a (sub)attosecond scale those pulses accurately represent the transverse electric fields in fast ion-atom collisions. Indeed, a momentum distribution closely resembling Fig. 4(b) has been observed in fast U^{92+} on He collisions [26].

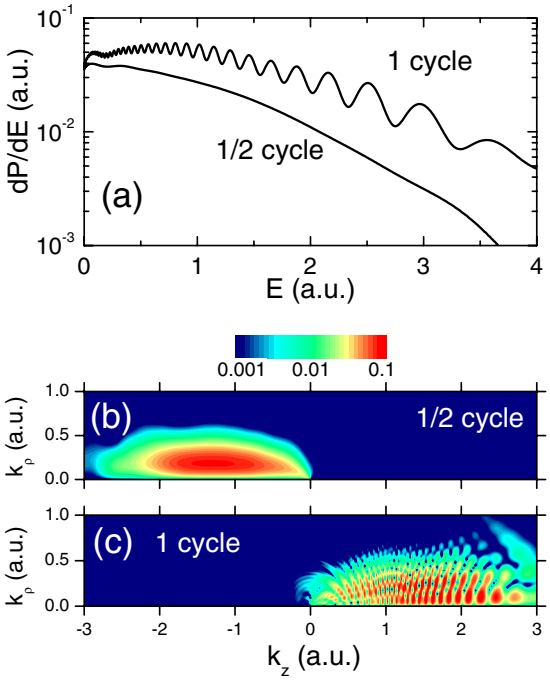

FIG. 4. (Color online) (a) *Ab initio* photoelectron spectra for the case of the electric field in Fig. 1(a): after a half-cycle pulse ($\tau=\pi/\omega$) and one-cycle pulse ($\tau=2\pi/\omega$). (b) *Ab initio* doubly differential electron momentum distribution after the half-cycle pulse (one slit). (c) *Ab initio* doubly differential electron momentum distribution after the one-cycle pulse (two slits).

We present in Fig. 5 the corresponding 2D momentum image for the one-cycle pulse calculated from the semiclassical model [Eq. (9)] and [Eq. (10)]. We observe a qualitative agreement with the *ab initio* results of Fig. 4. The photoelectron spectrum calculated with the semiclassical model in Fig. 5(a) reproduces the oscillating structure of the *ab initio* calculations in Fig. 4(a). Similarly, the 2D momentum distribution [Fig. 5(b)] qualitatively resembles the one extracted from the *ab initio* calculation [Fig. 4(c)]. For a more quanti-

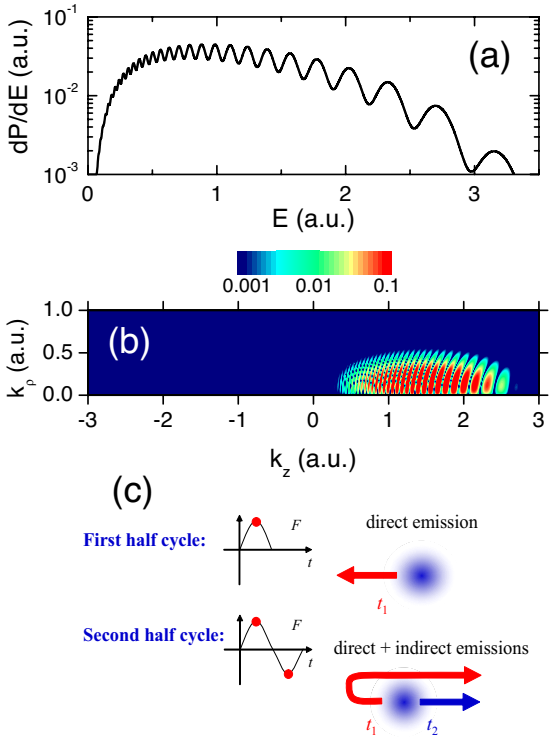

FIG. 5. (Color online) (a) Semiclassical photoelectron spectrum corresponding to the field in Fig. 1(a). (b) Semiclassical doubly differential electron momentum distribution after the pulse. (c) Schematic diagram of the interference process.

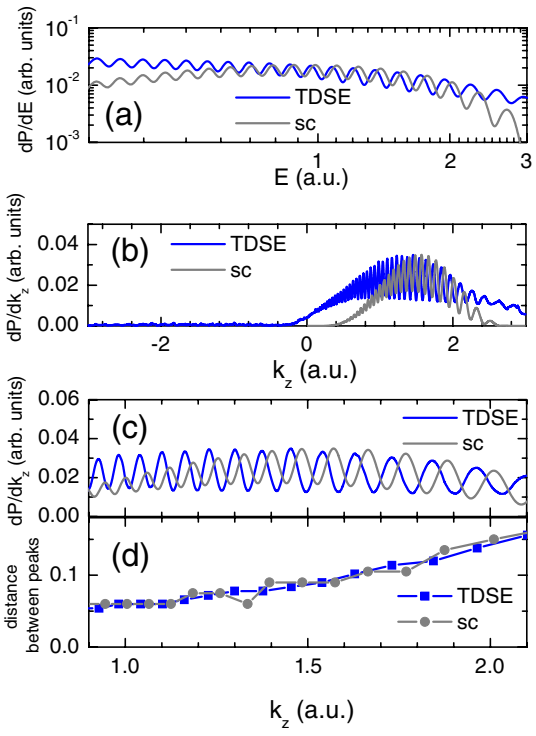

FIG. 6. (Color online) (a) Photoelectron spectra by solving the TDSE removing the excited states and by using the semiclassical (sc) model corresponding to the field in Fig. 1(a). (b) Longitudinal momentum distributions by the two methods. (c) Close-up of (a) showing the phase shift between two consecutive peaks. (d) Distance between two consecutive peaks of the longitudinal momentum distribution of (c).

tative comparison we show in Fig. 6 the results of both *ab initio* and semiclassical calculations as a function of energy [Fig. 6(a)] and longitudinal momentum [Figs. 6(b) and 6(c)]. In order to highlight the interferences in the final continuum states due to the two slits, we have removed in the *ab initio* calculations of Fig. 6 the contributions from intermediate excited states that are absent in the semiclassical calculation. We eliminate the contribution from excited states by setting their probability amplitudes to be zero at each time step in the propagation of the wave packet when solving the TDSE. The obvious drawback is the loss of unitarity of the time evolution. The interference peaks in the photoelectron spectrum and the momentum distribution are now more enhanced since they are not masked by the ionization coming from other bound states. Nevertheless, the distributions of Fig. 6 are very similar to the one with the full spectrum (Fig. 4), thereby ruling out the dominance of so-called Freeman resonances in causing the nonequidistant peaks in the energy spectrum over the range of energies considered. The agreement in the position of the peaks of the semiclassical energy spectrum and the TDSE one is reasonable, and the agreement in the separation of consecutive peaks in the longitudinal momentum distribution, shown in Fig. 6(d), proves the interference nature of the pattern.

The differences of the semiclassical model to the *ab initio* calculation are, however, significant and provide key insights into the emission process and its semiclassical description. The semiclassical model fails near threshold and at high energies. Classically, trajectories with final energies above $E=2\left(\frac{F_0}{\omega}\right)^2=4.5$ are not allowed [see also Fig. 6(a)]. Since the semiclassical approximation requires classical trajectories as input [Eqs. (9) and (11)], it must fail near the classical boundary of allowed trajectories and when the quantum mechanical emission probability extends into the classically forbidden region. There are also significant discrepancies at very low energies and negative longitudinal momenta $k_z<0$. The latter is due to the fact that classical trajectories do not reach this region. The classical longitudinal momentum distribution is strictly restricted to $0<k_z<\frac{2F_0}{\omega}=3$.

At low energies the discrepancy is, however, not primarily due the failure of classical dynamics but is the result of the additional approximation entering the present semiclassical model: namely, the neglect of the atomic core (i.e., Coulomb) potential in the SFA. This observation suggests the following interpretation of the diffraction images seen in Figs. 4(c) and 5(b): The diffraction image [Fig. 5(b)] is the result of the superposition of the direct emission from the point source, the atom, into the half-space of positive k_z and the indirect beam that is emitted from the point source in opposite direction, turned around by the field and also emitted in the positive half space [see Fig. 5(c) for a schematic diagram of the process]. The interference pattern is therefore controlled by the phase acquired by the redirected trajectory during the propagation in the (strong) field relative to that of the directly emitted wave packet. By contrast, the interference pattern of the full numerical solution [Fig. 4(c)] contains the additional phase acquired by the (re)scattering at the

atomic core potential, in the present case the Coulomb potential. In other words, while the semiclassical interference pattern is a holographic momentum image of the strong field acting on the rescattered wave packet, the full solution can be viewed as a holographic image of the combined atomic core potential and the strong field. In turn, the difference between the two images should provide direct information on the atomic scattering potential. This is illustrated in Fig. 6(c) where the phase shift along the k_z direction is displayed. This shift is due to the effect of the Coulomb potential on the ejected electron which is present in the *ab initio* calculations but is neglected in the semiclassical model (SFA).

IV. CONCLUSIONS

In this article we have presented theoretical studies on the interference effect observed in the electron distributions of ionized hydrogen atoms subject to a linearly polarized ultrashort one- and two-cycle laser pulse. We have extended the previous analysis in the energy domain to the full two-dimensional momentum space distribution. The two-dimensional electron momentum distribution after a full-cycle pulse evidences interference fringes. We have identified the peak structure in the photoelectron spectrum and the longitudinal momentum distribution as the interference phenomenon between the wave packets released at the first and second half-cycles, each half-cycle operating as an independent slit. In the understanding of the interference phenomenon we have made use of a simplified semiclassical model which has the advantage of being analytical. The semiclassical model partially reproduces the interference patterns in the spectra of ejected electrons. The differences in the pattern between semiclassical and *ab initio* calculations are mainly due to the Coulombic core. The present results suggest the feasibility of holographic imaging of the potential at which the laser driven wave packet rescatters.

ACKNOWLEDGMENTS

This work was supported by Grant Nos. SFB 016 ADLIS and P15025-N08 of FWF (Austria) and by EU Project No. HPRI-2001-50036. D.G.A. also acknowledges support by CONICET, Argentina.

[1] G. G. Paulus, W. Nicklich, F. Zacher, P. Lambropoulos, and H. Walther, J. Phys. B **29**, L249 (1996).
[2] T. Brabec and F. Krausz, Rev. Mod. Phys. **72**, 545 (2000); R. Kienberger, E. Goulielmakis, M. Uiberacker, A. Baltuska, V. Yakovlev, F. Bammer, A. Scrinzi, Th. Westerwalbesloh, U. Kleinberg, U. Heinzmann, M. Drescher, and F. Krausz, Nature (London) **427**, 817 (2004).
[3] P. Johnsson, R. Lopez-Martens, S. Kazamias, J. Mauritsson, C. Valentin, T. Remetter, K. Varju, M. B. Gaarde, Y. Mairesse, H. Wabnitz, P. Salieres, Ph. Balcou, K. J. Schafer, and A. L'Huillier, Phys. Rev. Lett. **95**, 013001 (2005).
[4] R. Moshammer *et al.*, Phys. Rev. Lett. **91**, 113002 (2003); R. Wiehle, B. Witzel, H. Helm, and E. Cormier, Phys. Rev. A **67**, 063405 (2003); J. Chen and C. H. Nam, *ibid.* **66**, 053415 (2002); J. Chen, J. Liu, L. B. Fu, and W. M. Zheng, *ibid.* **63**, 011404(R) (2000).
[5] G. G. Paulus, F. Grasbon, H. Walther, P. Villoresi, M. Nisoli, S. Stagira, E. Priori, and S. De Silvestri, Nature (London) **414**, 182 (2001); A. Apolonski *et al.*, Phys. Rev. Lett. **92**, 073902 (2004).
[6] Christian Per Juul Martiny and Lars Bojer Madsen, Phys. Rev. Lett. **97**, 093001 (2006).
[7] K. I. Dimitriou, D. G. Arbó, S. Yoshida, E. Persson, and J. Burgdörfer, Phys. Rev. A **70**, 061401(R) (2004).
[8] D. G. Arbó, S. Yoshida, E. Persson, K. I. Dimitriou, and J. Burgdörfer, Phys. Rev. Lett. **96**, 143003 (2006).
[9] A. Rudenko, K. Zrost, C. D. Schröter, V. L. B. de Jesus, B. Feuerstein, R. Moshammer, and J. Ullrich, J. Phys. B **37**, L407 (2004).
[10] C. M. Maharjan, A. S. Alnaser, I. Litvinyuk, P. Ranitovic, and C. L. Cocke, J. Phys. B **39**, 1955 (2006).
[11] F. H. M. Faisal and Schlegel, J. Phys. B **38**, L223 (2005).
[12] J. Chen, J. Liu, L. B. Fu, and W. M. Zheng, Phys. Rev. A **63**, 011404(R) (2000).
[13] F. Lindner, M. G. Schätzel, H. Walther, A. Baltuška, E. Goulielmakis, F. Krausz, D. B. Milošević, D. Bauer, W. Becker, and G. G. Paulus, Phys. Rev. Lett. **95**, 040401 (2005).
[14] N. B. Delone and V. P. Krainov, J. Opt. Soc. Am. B **8**, 1207 (1991).
[15] M. Lewenstein, K. C. Kulander, K. J. Schafer, and P. H. Bucksbaum, Phys. Rev. A **51**, 1495 (1995); M. Lewenstein, Ph. Balcou, M. Yu. Ivanov, A. L'Huillier, and P. B. Corkum, *ibid.* **49**, 2117 (1994).
[16] C. C. Chirila and R. M. Potvliege, Phys. Rev. A **71**, 021402(R) (2005).
[17] X.-M. Tong and S. I. Chu, Chem. Phys. **217**, 119 (1997).
[18] S. Dionissopoulou, Th. Mercouris, A. Lyras, and C. A. Nicolaides, Phys. Rev. A **55**, 4397 (1997).
[19] O. Schöller, J. S. Briggs, and R. M. Dreizler, J. Phys. B **19**, 2505 (1986).
[20] A. Messiah, *Quantum Mechanics 1* (North-Holland, New York, 1965); S. Dionissopoulou, Th. Mercouris, A. Lyras, and C. A. Nicolaides, Phys. Rev. A **55**, 4397 (1997).
[21] G. Arfken, *Mathematical Methods for Physicist* (Academic Press, New York, 1985).
[22] P. B. Corkum, N. H. Burnett, and M. Y. Ivanov, Opt. Lett. **19**, 1870 (1994); M. Ivanov, P. B. Corkum, T. Zuo, and A. Bandrauk, Phys. Rev. Lett. **74**, 2933 (1994).
[23] R. R. Jones, D. You, and P. H. Bucksbaum, Phys. Rev. Lett. **70**, 1236 (1993).
[24] J. Burgdörfer, Nucl. Instrum. Methods Phys. Res. B **42**, 500 (1989); M. Melles, C. O. Reinhold, and J. Burgdörfer, Nucl. Instrum. Methods Phys. Res. B **79**, 109 (1993); C. O. Reinhold, J. Burgdörfer, M. T. Frey, and F. B. Dunning, Phys. Rev. Lett. **79**, 5226 (1997).
[25] E. Persson, K. Schiessl, A. Scrinzi, and J. Burgdörfer, Phys. Rev. A **74**, 013818 (2006).
[26] R. Moshammer *et al.*, Phys. Rev. Lett. **79**, 3621 (1997).